



## Singular fractional technique for free convective Casson hybrid nanofluid with optically thick medium and shape effects

N M Lisha & A G Vijaya Kumar\*

Department of Mathematics, School of Advanced Sciences, Vellore Institute of Technology, Vellore, Tamil Nadu-632 014, India

\*E-mail: vijayakumarag@vit.ac.in

*Received 25 February 2023; accepted 16 May 2023*

The transmission of heat in a time-dependent flow of a viscid non-Newtonian hybrid nanofluid comprising magnetite and copper oxide nanoparticles persuaded by an upright plate has been explored in regards to the effect of heat radiation and nanoparticle shape factors. The fluid flow phenomenon of the problem is constructed using the derivative of the Caputo fractional order  $0 < \alpha < 1$ . As a hybrid method, the dimensionless governing fractional partial differential equation was solved analytically using transforms such as Laplace and Fourier sine. With the Mittag-Leffler function, analytical solutions are achieved for fluid flow, energy distribution, rate of heat transmission, and shear stress. Moreover, limit-case solutions for classical PDEs were given for the derived governing flow model. Graphical depictions, tables, and bar graphs are constructed using "MATLAB" for a thorough examination of the problem. The graphical findings suggest that the efficiency of hybrid nanofluids is substantially better with the Caputo fractional order approach than with ordinary derivatives. Finally, a comparison with existing literature results is performed and determined to be good.

**Keywords:** Caputo fractional derivative, Fourier sine transform, Laplace transform, Mittag-Leffler function, Optically-thick medium, Thermal radiation

Heat transfer fluid is essential in the heating and cooling of several manufacturing industries. Even though there is an increasing need for energy-saving home appliances, efficient fluid heat transport is still difficult to achieve. Common fluids, including ethylene glycol, water and oil have poor heat transfer capabilities owing to their low heat capacities. Choi and Eastman<sup>1</sup> employed nano-sized particles for the first time in 1995 to improve the heat transmission of such fluids, and the resulting fluid is referred to as a nanofluid. Nanofluids are being investigated as a possible means of improving the performance of heat transfer fluids. This innovative idea of nanofluids shows that their thermal conductivity is several times greater than that of base fluids. Since then, a large variety of various sorts of equipment have been created for a broad spectrum of useful applications in different sectors such as solar ponds, engineering<sup>2</sup>, aircraft, heat exchanger<sup>3</sup>, and cancer therapy. Some of the recent development in field of nanofluid are observed in the studies<sup>4,5,6</sup>. Most of the industry's demands have been met by the invention of nanofluids; nevertheless, the dispersion of mono-nanomaterials doesn't have the needed influence on thermal efficacy. As a result, researchers have been

working hard to develop a fluid that is both superior and more effective. In 1989, Yamanda<sup>7</sup> developed a more efficient type of nanofluid by mixing two or more nanomaterials with varying properties with ordinary fluids. Hybrid nanofluid, an upgraded classification of nanofluid, indicates the potential for increases in thermal efficiency, which is used in many different industries, including solar energy, biomedicine<sup>8</sup>, spray cooling systems, radiators, heat exchangers<sup>9</sup> and so on. To further enhance the heat transfer characteristics of individual nanofluids and to advantageously combine distinct qualities from oxides, carbon nanotubes, metals, composites, etc., the use of hybrid nanofluids has been proposed. The advantage of employing hybrid nanofluids is to further enhance their heat transfer and pressure drop characteristics. This will be accomplished by striking a balance between the benefits and drawbacks of using individual suspensions. This balance will be achieved due to the hybrid nanofluids' excellent aspect ratio, improved thermal network, and synergistic impact of nanomaterials. In conclusion, the hybrid nanofluids that included composite nanoparticles were shown to provide a considerable increase in thermal conductivity. However, the cost of

nanofluids as well as their long-term stability, manufacturing method, selection of appropriate nanomaterial combinations to produce synergistic impact, and other potential issues may be key obstacles to actual applications. Many researchers have studied the flow and transmission of heat for different hybrid nanofluids in a variety of morphologies and operating circumstances. Rizwan Ali<sup>10</sup> reviewed the power law memory of a hybrid nanofluid subject to a pressure difference using a fractional derivative. Muhammad Saqib<sup>11</sup> developed a fractional derivative technique to study heat transmission in hybrid nanofluid copper and alumina on two vertical parallel plates. Sami Ul Haq<sup>12</sup> utilized a Caputo Fabrizio derivative to examine a Casson hybrid nanofluid with an oscillatory surface. Mumtaz Khan<sup>13</sup> extensively analyzed the transport of heat in an unstable MHD flow of second grade hybrid fluids along an inclined plane embedded in a Darcy media.

Thermal radiation is the release of heat energy from a radiating material in the form of electromagnetic waves. Heat radiation is essential for producing high temperatures. Many important engineering processes, including those in nuclear power plants, furnace design, gas-cooled nuclear reactors, missile reentry, metallic rolling, rocket combustion, fins, various aircraft and satellite propulsion devices, space vehicles, etc., occur at high temperatures, where the effect of heat radiation is crucial. Numerous researchers have focused on the magnetohydrodynamic convection of nanofluids to examine the effect of radiation in a variety of geometries and setups. Bharath Kumar<sup>14</sup> studied the joule-heated and thermally radiated MHD flow of Eyring-Powell nanofluid in an inclinable, porous, stretched sheet. Bilal Jamil<sup>15</sup> investigated the impacts of heat radiation and chemical processes on the unstable Maxwell flow with constant densities triggered by impetuous surface extending. It was observed that the non-integer derivative enhanced the flow. S. Maiti<sup>16</sup> proposed a non-Newtonian Casson fluid to describe the non-integer order time derivative of flow of blood in arteries subjected to MHD and heat radiation. Syed Tauseef Saeed<sup>17</sup> explore the time-dependent MHD Oldroyd-B fluid and find that the ABC method out performs other fractional models due to the influences of the heat source, heat radiation with ramped wall velocity and temperature. Ridhwan Reyaz<sup>18</sup> presented the influence of thermal radiation on the magnetohydrodynamic non-Newtonian fluid in a vertically rotating surface.

To investigate non-Newtonian fluid behaviour, several different component equations have been proposed and utilized in a broad spectrum of industries and fields of research. Non-Newtonian liquids often exhibit characteristic stress variations. One such liquid with many applications in industry and engineering is Casson fluid. In 1959, Casson developed the Casson<sup>19</sup> fluid model. Casson fluid is an infinitely viscous shear-thinning liquid with zero shear stress. The Casson fluid begins to move when the yield stresses are less than the shear stresses. Toothpaste, slurries, tomato sauce, fruit liquids, blood, and soup are examples of Casson fluid. As a result, Casson fluids are used in pharmaceuticals, cosmetics, polymer processing industries and many more. Suripeddi Srinivas<sup>20</sup> explored a flow of non-Newtonian nanofluid in a porous stretchable surface. Muhammad Arif<sup>21</sup> used a water-based ternary hybrid nanofluid to analyze the heat transfer study of a radiator. They discovered an increment in the rate of heat transport of 33.67 percent. Fuzhang Wang<sup>22</sup> swotted the unstable thermal flow of Casson fluid using extended Fourier's law and Prabhakar's fractional derivative. Noman Sarwar<sup>23</sup> provided the Prabhakar non-integer flow model for rotating surfaces using Laplace transformation techniques. Veera Krishna<sup>24</sup> investigated the Laplace technique to analyses the magnetohydrodynamic Casson fluid flow across an infinite exponential hastened upright permeable plate. J. Kayalvizhi<sup>25</sup> deals with the nanofluid flow of heat transfer along an upright plane using a fractional approach.

Different mathematical methods are used to solve PDEs of non-integer order models in the research. Both non-local integration and differentiation are topics of study in the field of fractional calculus. Fractional calculus has found widespread usage in mathematical modelling and the study of numerous physical phenomena. To optimize these mathematical models and numerical outcomes, the fractional derivative is the most efficient approach. Rheology, fluid flows, electrical networks, electromagnetic theory, viscoelastic materials, and diffusive transport are just a few examples of the kind of real-world issues that might benefit from the clarity provided by fractional derivative models. The investigations of hybrid nanofluids based on ordinary derivatives have constraints and certain restrictions in solving and analyzing the fractional ordered PDEs, as well as some memory effect challenges. Different fractional derivative approaches may be used to improve and

study the memory effects on the behaviour of hybrid nanofluids. Different fractional-order definitions, such as Riemann-Liouville<sup>26</sup>, Caputo<sup>27</sup>, Caputo-Fabrizio<sup>28</sup>, and Atangana-Baleanu<sup>29</sup>, were utilized to solve many physical and numerical phenomena. Talha Anwar<sup>30</sup> look at the impacts of ramped heating and heat generation/absorption on the hybrid nanofluid radiative flows across an inclined surface. Ali Raza<sup>31</sup> explored an analytical solution for fractional nanofluids subjected to heat flux and radiation effects, with the conclusion that the fractional derivatives behave quite differently from typical nanofluids. Jawad Ahmad<sup>32</sup> explore the Jeffrey nanofluid magnetohydrodynamic flow in a horizontal channel. They revealed that Ag nanoparticles enhance the rate of heat transfer of engine oil by 24.80% while Cu nanoparticles increase it by 16.910 percent. Dolat Khan<sup>33</sup> examined the application of the water filtering process using fractional mathematical analysis of hybrid nanofluid in the presence of porous media and heat production. They determined that the shape of nanoparticles in the form of a blade increases heat transmission by up to 11.14983%. Muhammad Saqib<sup>34</sup> investigate the application of the Atangana-Baleanu fractional derivative employing CNTs nanofluid on a vertical plate, and they discover that the memory effect lessens as fractional parameters increase. Muhammad Danish Ikram<sup>35</sup> utilized the Laplace transformation method to analyze the hybrid nanofluid in a microchannel with MHD and a heat source, and the findings were represented as an M-function. Lisha and Vijayakumar<sup>36</sup> used the Caputo fractional approach to study the effects of the rate of heat transfer on a Casson fluid in a magnetohydrodynamic flow past a vertical surface.

Based on the above information, it stands out as a gap in the literature that no previous work has attempted to fill by studying thermal radiation, shape variables, and hybrid nanofluids with the use of the Caputo derivative. So, the present research intends to expand on Ndolane Sene's<sup>37</sup> work by adopting thermal radiation and different shapes of a hybrid nanofluid model employing magnetite, copper oxide as nanoparticles, and water as the base fluid through an infinite upright plate. The Caputo derivative model has the advantage of accounting for the so-called memory effect, whereby the derivative of a constant function yields zero. The novel part will be the execution of the Caputo fractional derivative and its technique for achieving the exact solution. Furthermore, free convection occurs as a result of the

buoyancy effect, and the energy equation is improved by including heat radiation. Because of the coupling and non-linearity of the governing equations, the momentum equation is formulated using the Boussinesq approximation. Depending on the physical conditions, we employed an exact solution, namely the Laplace and Fourier sine transform methods, to transform non-linear governing partial differential equations into ODEs. These precise solutions are provided for the energy and velocity fields of a hybrid nanofluid. The impact of physical factors with distinct fraction orders on the fractional temperature and momentum of a hybrid nanofluid is examined by visualizing energy and velocity curves. Also, the effects of various factors on thermal properties and fluid flow were studied and shown in graphs and tables. Using this model has real-world applications in parabolic trough solar collectors, as an effective adsorbent for removing dyes from waste water, in biomechanical applications such as radiation therapy for lung cancer treatment, and in using magnetic field intensity to control blood flow during surgeries.

### Mathematical Description

Consider an optically thick radiating water-based hybrid nanofluid (Magnetite and Copper oxide) positioned vertically upward is taken into consideration in the present study. For the analysis, the rectilinear coordinate system is chosen, and the flow is considered on the y-axis while its x-axis is set to be normal to the surface. Since it is assumed that the fluid is moving along the y axis, the physical parameters are solely dependent on the x and t coordinates. The fluid is viscous, incompressible, conducting, and non-electrified. It is considered that the fluid is gray, absorbs, emits radiation, and acts as a non-scattered medium. To simplify the energy and velocity equations, viscous dissipation and pressure gradient are ignored. To produce hybrid nanofluid, distinct nanoparticle shapes (hexahedron, tetrahedron, cylinder, blade, and lamina) are suspended in the host fluid. Both the surface and the hybrid nanofluid are in stable state at  $\tau = 0$ . As time goes on, the fluid moves forward at a speed of U, and its temperature rises to  $T_w$ . Due to the change in temperature, body force shows up in this situation as buoyant force. In addition to this, the flow behavior of the hybrid nanofluid is examined with the help of the Brinkman fluid model. Fig. 1 shows the problem's flow geometry.

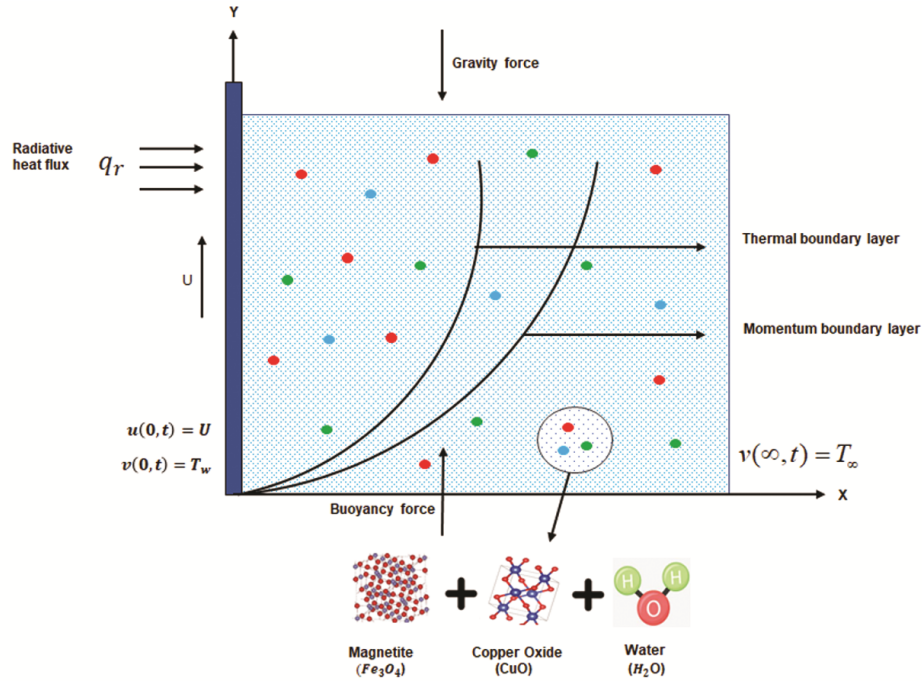


Fig. 1 — Visualization of the flow model and the coordinate system

The rheological equation for an inviscid Casson fluid is expressed in the following form (S. A. Shehzad<sup>38</sup>)

$$\left. \begin{aligned} \pi_{i,j} &= 2(\mu_\gamma + \frac{p_y}{\sqrt{2\pi}})e_{ij} \quad \text{when } \pi > \pi_c \\ \pi_{i,j} &= 2(\mu_\gamma + \frac{p_y}{\sqrt{2\pi_c}})e_{ij} \quad \text{when } \pi < \pi_c \end{aligned} \right\} \dots (1)$$

Here  $\pi = e_{ij}e_{ij}$  where  $e_{ij}$  represents  $(i, j)^{th}$  component of the deformation,  $\mu_\gamma$  represents the plastic dynamic viscosity,  $p_y$  symbolizes the yields stress,  $\pi$  is the product of the component of deformation with itself and  $\pi_c$  is the critical value of this product.

The Rosseland approximation (Nandkeolyar<sup>39</sup>) describes the radiative heat flow  $q_r$  in such a way that

$$q_r = -\frac{4\sigma^*}{3k^*} \frac{\partial T^{*4}}{\partial x^*} \dots (2)$$

where  $k^*, \sigma^*$  signifies the coefficient of absorption and the Stefan-Boltzmann constant, respectively.

It should be emphasized that the study is confined to optically thick fluids based on the Rosseland

approximation. The energy equation is clearly non-linear in temperature  $T$ , yet it appears to be linear. It can now be linearized by taking into consideration the small temperature variations inside the flow and extending  $T^{*4}$  with the aid of the Taylor series about  $T_\infty$  and ignoring higher order variables results in Eq (3).

$$T^{*4} \cong (4T^* - 3T_\infty^*)T_\infty^{*3} \dots (3)$$

Employing Eqs (2) and (3), we get the form of energy equation that characterizes linear radiative heat transfer. Under the aforementioned assumptions, the mathematical formulation of corresponding convectonal flow can be characterized by Boussinesq's approximation (Farhad Ali<sup>40</sup>) with the governing PDE's (Ndolane Sene<sup>37</sup>).

$$\frac{\partial u}{\partial x} + \frac{\partial v}{\partial y} = 0 \dots (4)$$

$$\rho_{hmf} \frac{\partial u}{\partial t} = (1 + \frac{1}{\beta})\mu_{hmf} \frac{\partial^2 u}{\partial x^2} + \rho_{hmf}\gamma_{hmf} g(T - T_\infty) \dots (5)$$

$$(\rho C_p)_{hmf} \frac{\partial T}{\partial t} = \kappa_{hmf} \frac{\partial^2 T}{\partial x^2} + \frac{16\sigma^* T_\infty^3}{3k^*} \frac{\partial^2 T}{\partial x^2} \dots (6)$$

The initial and boundary conditions in dimensional form are

$$\left. \begin{aligned} u(x, 0) = 0, T(x, 0) = T_\infty \\ u(0, t) = U, T(0, t) = T_w \\ u(\infty, t) \rightarrow 0, T(\infty, t) \rightarrow T_\infty \end{aligned} \right\} \dots (7)$$

Table 1 summarizes the thermo - physical aspects of hybrid nanofluids. The thermophysical attributes of the host fluid ( $H_2O$ ) and nanomaterials Magnetite ( $Fe_3O_4$ ), Copper Oxide ( $CuO$ ) are shown in Table 2. The shape factor for a variety of nanoparticles is shown in Table 3.

Buckingham's - pi ( $\pi$ ) theorem (W.D Curtis<sup>45</sup>) was employed to develop the dimensionless physical quantities that are described below.

$$\begin{aligned} u^* = \frac{u}{U}, x^* = \frac{U}{\nu} x, \tau^* = t \frac{U^2}{\nu}, v = \frac{T - T_\infty}{T_w - T_\infty} \\ Pr = \frac{(\mu C_p)_f}{\kappa_f}, Gr = \frac{g \nu_f \gamma_f (T_w - T_\infty)}{U^3}, R = \frac{16 \sigma^* T_\infty^3}{3k^* k_f} \dots (8) \end{aligned}$$

When Eqs. (4) - (7) are transformed using the non-dimensional quantities provided in Eq (8) and the \* sign is omitted, a concise version of the dimensionless fractional governing partial differential equations (Ndolane Sene<sup>37</sup>) is obtained as follows:

$$D_\tau^\alpha u = A_7 \left(1 + \frac{1}{\beta}\right) \frac{\partial^2 u}{\partial x^2} + A_9 Gr v \dots (9)$$

$$D_\tau^\alpha v = \frac{A_{10}}{Pr} \frac{\partial^2 v}{\partial x^2} \dots (10)$$

where the fractional derivative of Caputo<sup>27</sup> is stated as

$$D_C^\alpha f(t) = \frac{1}{\Gamma(1-\alpha)} \int_0^t (t-s)^{-\alpha} \frac{df(s)}{ds}; 0 < \alpha < 1, t > 0 \dots (11)$$

and the Laplace transformation of  $D_C^\alpha f(t)$  is

$$L[D_C^\alpha f(t)] = L[f(t)]s^\alpha - f(0)s^{\alpha-1} \dots (12)$$

The required dimensionless initial and boundary condition are as follows.




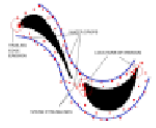

Table 1 — Thermophysical characterization of hybrid nanofluids (Talha Anwar<sup>41</sup>)

Properties	Hybrid nanofluid
Viscosity, $\mu$	$\mu_{hmf} = \frac{\mu_f}{(1 - \phi_{Fe_3O_4})^{2.5} (1 - \phi_{CuO})^{2.5}}$ (Brinkman model)
Density, $\rho$	$\rho_{hmf} = [\rho_f (1 - \phi_{Fe_3O_4}) + \phi_{Fe_3O_4} \rho_{Fe_3O_4}] (1 - \phi_{CuO}) + \rho_{CuO} \phi_{CuO}$
Specific heat capacity, $C_p$	$(\rho C_p)_{hmf} = [\phi_{Fe_3O_4} (\rho C_p)_{Fe_3O_4} + (1 - \phi_{Fe_3O_4}) (\rho C_p)_f] (1 - \phi_{CuO}) + (\rho C_p)_{CuO} \phi_{CuO}$
Thermal conductivity, $\kappa$	$\kappa_{hmf} = \kappa_{nf} \left[ \frac{\kappa_{CuO} + (n-1)\kappa_{nf} - (n-1)(\kappa_{nf} - \kappa_{CuO})\phi_{CuO}}{\kappa_{CuO} + (n-1)\kappa_{nf} + (\kappa_{nf} - \kappa_{CuO})\phi_{CuO}} \right]$ (Maxwell model) where $\kappa_{nf} = \kappa_f \left[ \frac{\kappa_{Fe_3O_4} + (n-1)\kappa_f - (n-1)(\kappa_f - \kappa_{Fe_3O_4})\phi_{Fe_3O_4}}{\kappa_{Fe_3O_4} + (n-1)\kappa_f + (\kappa_f - \kappa_{Fe_3O_4})\phi_{Fe_3O_4}} \right]$
Thermal expansion coefficient, $\gamma$	$(\rho\gamma)_{hmf} = [(1 - \phi_{Fe_3O_4})(\rho\gamma)_f + \phi_{Fe_3O_4}(\rho\gamma)_{Fe_3O_4}] (1 - \phi_{CuO}) + (\rho\gamma)_{CuO} \phi_{CuO}$

Table 2 — Host fluid and nanoparticle thermophysical features (Ali and Sandeep<sup>42</sup>, Kumaresan<sup>43</sup>)

Physical properties	Water ( $H_2O$ )	Magnetite ( $Fe_3O_4$ )	Copper Oxide ( $CuO$ )
$\rho / Kgm^{-3}$	997.1	5180	6320
$C_p / JKg^{-1}K^{-1}$	4179	670	531.8
$\kappa / Wm^{-1}K^{-1}$	0.613	9.7	76.5
$\gamma / K^{-1}$	$210 \times 10^{-6}$	$0.74 \times 10^{-6}$	$1.80 \times 10^{-5}$
Pr	6.2	-	-

Table 3 — Shape factor of different nanoparticle (Umar Farooq<sup>44</sup>)

Shape of nanoparticle	Model	$p$
Hexahedron		3.7221
Tetrahedron		4.0613
Cylinder		4.9
Blade		8.3
Lamina		16.1576

$$\begin{aligned} \tau \leq 0: & \quad u = 0, v = 0 \forall x > 0 \\ \tau > 0: & \quad \begin{aligned} u = 1, v = 1: x = 0 \\ u \rightarrow 0, v \rightarrow 0: x \rightarrow \infty \end{aligned} \end{aligned} \quad \dots (13)$$

where  $A_1 = \left[ \frac{\kappa_{p_2} + (n-1)\kappa_{nf} - (n-1)(\kappa_{nf} - \kappa_{p_2})\phi_2}{\kappa_{p_2} + \kappa_{nf}(n-1) + (\kappa_{nf} - \kappa_{p_2})\phi_2} \right]$ ,

$$A_2 = \frac{k_{p_1} + k_f(n-1) - (k_f - k_{p_1})(n-1)\phi_1}{k_{p_1} + (n-1)k_f - (k_f - k_{p_1})\phi_1},$$

$$A_3 = (1 - \phi_2) \left[ (1 - \phi_1) + \phi_1 \frac{(\rho C_p)_{p_1}}{(\rho C_p)_f} \right] + \left[ \frac{(\rho C_p)_{p_2}}{(\rho C_p)_f} \right] \phi_2,$$

$$A_4 = \frac{A_1 A_2}{A_3},$$

$$A_5 = (1 - \phi_1)^{2.5} (1 - \phi_2)^{2.5},$$

$$A_6 = (1 - \phi_2) \left[ (1 - \phi_1) + \phi_1 \frac{\rho_{p_1}}{\rho_f} \right] + \left[ \frac{\rho_{p_2}}{\rho_f} \right] \phi_2, \quad A_7 = \frac{1}{A_5 A_6},$$

$$A_8 = (1 - \phi_2) \left[ (1 - \phi_1) + \phi_1 \frac{(\rho \gamma)_{p_1}}{(\rho \gamma)_f} \right] + \left[ \frac{(\rho \gamma)_{p_2}}{(\rho \gamma)_f} \right] \phi_2,$$

$$A_9 = \frac{A_8}{A_6}, \quad A_{10} = A_4 + \frac{R}{A_3}$$

**Method for solution**

There are several possible ways to solve the fractional (non-integer) differential equations that are given in Eqs. (9) and (10). We will discuss how to apply analytical methods to the problem of finding results. The Fourier sine and Laplace transformations are employed in order to obtain accurate answers for our existing model. The following research articles<sup>46,47</sup> discuss this method in further detail. This approach is advantageous in this research since it enables the formulation of linear non-integer differential equations. Before we begin the solution, we describe the technique used in this work:

- To solve the governing equation for momentum and temperature first implement the Fourier sine transformation on both sides of the equations.
- Secondly, use the Laplace transformation to the obtained equation.
- Employ the inversion of the Laplace transformation. After employing inverse Laplace transform, to solve the right hand side of the equation use Mittag-Leffler function.
- Finally, the equation reduced to the form of Mittag-Leffler function then inverse Fourier sine transform is applied which yields to the exact solution.

**Fractional temperature distribution calculation**

Eq. (10) has been utilized to solve the fractional temperature equation using boundary conditions provided by Eq (13).

The initial stage of this method is applying the Fourier sine transform to Eq. (10) and is obtained as follows:

$$F_s [D_\tau^\alpha v(x, \tau)] = F_s \frac{A_{10}}{pr} \left[ \frac{\partial^2 v(x, \tau)}{\partial x^2} \right] \quad \dots (14)$$

$$D_\tau^\alpha v(q, \tau) = \frac{A_{10}}{pr} [qv(0, \tau) - q^2 v(q, \tau)] \quad \dots (15)$$

where the Fourier sine function is q and the Fourier sine transform is represented by  $F_s$ .

The next step of the method is to apply the Laplace transform to Eq. (15) and then use Eq. (13) to get

$$L[D_t^\alpha v(q, \tau)] = \frac{A_{10}q}{Pr} L[v(0, \tau)] - \frac{A_{10}q^2}{Pr} L[v(q, \tau)] \quad \dots (16)$$

Eq. (16) is rearranged here as follows

$$v(q, s) = \frac{qA_{10}}{Pr} \left[ \left( \frac{1}{s} - \frac{s^{\alpha-1}}{s^\alpha + \frac{q^2 A_{10}}{Pr}} \right) \frac{Pr}{q^2 A_{10}} \right] \quad \dots (17)$$

Eq. (17) can be solved using the inverse of the Laplace transformation, which results in the given equation.

$$v(q, \tau) = \frac{1}{q} \left[ 1 - L^{-1} \left[ \frac{s^{\alpha-1}}{s^\alpha + \frac{q^2 A_{10}}{Pr}} \right] \right] \quad \dots (18)$$

Analytical solution to Eq. (18) is obtained by using the Mittag-Leffler function (Podlubny<sup>48</sup>).

The series provides the definition for the Mittag-Leffler function as

$$E_{\alpha, \beta}(z) = \sum_{k=0}^{\infty} \frac{z^k}{\Gamma(\alpha k + \beta)} \quad \dots (19)$$

Here  $\alpha, \beta \in \mathbb{C}$ ,  $\Re(\alpha) > 0$ ,  $\Re(\beta) > 0$  and  $z \in \mathbb{C}$ , where  $\mathbb{C}$  is the set of complex numbers.

As a result of doing it,  $\beta = 1$ ,  $z = -\lambda \tau^\alpha$  and  $\lambda = \frac{q^2 A_{10}}{Pr}$  in Eq. (19), this is reduced to the form

$$E_\alpha \left( -\frac{q^2 A_{10}}{Pr} \tau^\alpha \right) = L^{-1} \left[ \frac{s^{\alpha-1}}{s^\alpha + \frac{q^2 A_{10}}{Pr}} \right] \quad \dots (20)$$

$$v(q, \tau) = \frac{1}{q} \left[ 1 - E_\alpha \left( -\frac{q^2 A_{10}}{Pr} \tau^\alpha \right) \right] \quad \dots (21)$$

When applied to Eq (21), the inverse of the Fourier sine yields the result

$$v(x, \tau) = 1 - \frac{2}{\pi} \int_0^\infty \frac{\sin qx}{q} E_\alpha \left( -\frac{q^2 A_{10} \tau^\alpha}{Pr} \right) dq \quad \dots (22)$$

### Fractional fluid flow distribution calculation

The Fourier sine transform is employed in Eq. (9) in order to solve the fractional velocity equation and it

is assumed  $\mu = 1 + \frac{1}{\beta}$  the modified equation is

$$F_s [D_t^\alpha u(x, \tau)] = F_s \left[ A_7 \mu \frac{\partial^2 u}{\partial x^2} + GrvA_9 \right] \quad \dots (23)$$

$$D_t^\alpha u(q, \tau) = A_7 \mu q u(0, \tau) - A_7 \mu q^2 u(q, \tau) + A_9 Grv(q, \tau) \quad \dots (24)$$

By applying Eq. (13) to Eq. (24) through the Laplace transform, we get

$$L[D_t^\alpha u(q, \tau)] = A_7 \mu q L[u(0, \tau)] - A_7 \mu q^2 L[u(q, \tau)] + A_9 GrL[v(q, \tau)] \quad \dots (25)$$

with more simplifications Eq. (25), which transforms to

$$u(q, s) = \frac{\mu q A_7}{s(s^\alpha + \mu q^2 A_7)} + \frac{GrqA_9 A_{10}}{spr(s^\alpha + \frac{q^2 A_{10}}{Pr})(s^\alpha + \mu q^2 A_7)} \quad \dots (26)$$

where

$$a(q, s) = \frac{\mu q A_7}{s(s^\alpha + \mu q^2 A_7)}, \quad (19)$$

$$b(q, s) = \frac{GrqA_9 A_{10}}{spr(s^\alpha + \mu q^2 A_7)(s^\alpha + \frac{A_{10} q^2}{Pr})}$$

The inversion of Laplace transformation is applied to Eq. (26)

$$L^{-1}[u(q, s)] = L^{-1} \left[ \frac{\mu q A_7}{s(s^\alpha + \mu q^2 A_7)} + \frac{GrqA_9 A_{10}}{spr(s^\alpha + \mu q^2 A_7)(s^\alpha + \frac{q^2 A_{10}}{Pr})} \right] \quad \dots (27)$$

$$a(q, \tau) = \frac{1}{q} [1 - E_\alpha(-q^2 \mu A_7 \tau^\alpha)] \text{ where } \lambda = A_7 \mu q^2$$

$$b(q, \tau) = \frac{GrA_9 A_{10} \tau^\alpha}{prq(\mu A_7 - \frac{A_{10}}{Pr})} \left[ E_{\alpha, \beta} \left( -\frac{q^2 A_{10}}{Pr} \tau^\alpha \right) - E_{\alpha, \beta}(-\mu q^2 A_7 \tau^\alpha) \right]$$

where  $\lambda = \frac{A_{10}q^2}{pr}$

The solution is written as a representation of the Mittag-Leffler function using the inverse Fourier transform.

$$a(x, \tau) = 1 - \frac{2}{\pi} \int_0^\infty \frac{\sin qx}{q} E_\alpha(-q^2 \mu A_7 \tau^\alpha) dq$$

$$b(x, \tau) = \frac{2GrA_9A_{10}}{k} \int_0^\infty \frac{\sin qx\tau}{q} \left[ E_{\alpha,\beta}(-\frac{q^2A_{10}}{pr} \tau^\alpha) - E_{\alpha,\beta}(-\mu q^2 A_7 \tau^\alpha) \right] dq$$

where  $k = pr\pi(A_7\mu - \frac{A_{10}}{pr})$

and the analytical result is  $u(x, \tau) = a(x, \tau) + b(x, \tau)$  ... (28)

**Limiting cases**

**Classical case with hybrid nano-particles temperature field**

The equation for temperature that corresponds to  $\alpha \rightarrow 1$  in Eq. (10) can be reduced to the form as

$$v(x, \tau) = \text{erfc}\left(\frac{x\sqrt{Pr}}{2\sqrt{\tau A_{10}}}\right) \dots (29)$$

where *erfc* is a Gaussian error function.

**Classical case with hybrid nano-particles flow field**

The equation for flow field that corresponds to  $\alpha \rightarrow 1$  in Eq. (9) can be reduced to the form as

$$u(x, \tau) = \text{erfc}\left(\frac{x}{2\sqrt{\tau B_1}}\right) - \frac{B_2}{B_1} \left[ \left( \tau + \frac{x^2}{2B_1} \right) \text{erfc}\left(\frac{x}{2\sqrt{\tau B_1}}\right) - x \sqrt{\frac{\tau}{\pi B_1}} e^{-\frac{x^2}{4\tau B_1}} \right] + \frac{B_2}{B_1} \left[ \left( \tau + \frac{x^2 pr}{2A_{10}} \right) \text{erfc}\left(\frac{x\sqrt{Pr}}{2\sqrt{\tau A_{10}}}\right) - x \sqrt{\frac{\tau pr}{\pi A_{10}}} e^{-\frac{x^2 Pr}{4\tau A_{10}}} \right]$$

where

$$B = 1 + \frac{1}{\beta}, B_1 = BA_7, B_2 = -\frac{A_9A_{10}B_1Gr}{B_1 Pr - A_{10}} \dots (30)$$

**Classical Casson fluid with hybrid nano-particles flow field**

The following equation is derived for the velocity field of a classical Casson fluid by replacing  $\beta \rightarrow \infty, \alpha \rightarrow 1$  in Eq. (9), we get

$$u(x, \tau) = \text{erfc}\left(\frac{x}{2\sqrt{\tau A_7}}\right) + B_3$$

$$B_3 \left[ \left( \tau + \frac{x^2}{2A_7} \right) \text{erfc}\left(\frac{x}{2\sqrt{\tau A_7}}\right) - x \sqrt{\frac{\tau}{\pi A_7}} e^{-\frac{x^2}{4\tau A_7}} \right] - B_3 \left[ \left( \tau + \frac{x^2 pr}{2A_{10}} \right) \text{erfc}\left(\frac{x\sqrt{Pr}}{2\sqrt{\tau A_{10}}}\right) - x \sqrt{\frac{\tau pr}{\pi A_{10}}} e^{-\frac{x^2 Pr}{4\tau A_{10}}} \right]$$

where  $B_3 = \frac{A_9A_{10}Gr}{A_7 Pr - A_{10}}$  ... (31)

**Physical quantities**

The heat transmission rate towards the solid boundary is calculated from the temperature field with regard to the penetration distance at the wall, which is represented in dimensionless notations as:

$$Nu = - \left[ \frac{\partial v}{\partial x} \right]_{x=0}$$

The Nusselt number (*Nu*) is calculated using Eq. (22), and an exact representation of the dimensionless heat transfer rate is given by

$$Nu = \sqrt{\frac{pr}{A_{10}}} \frac{\tau^{\frac{\alpha}{2}}}{\Gamma(1 - \frac{\alpha}{2})} \dots (32)$$

We examine skin friction (rate of velocity change in the flow with respect to x) from the velocity field, which is provided in a dimensionless equation as

$$C_f = - \left[ \frac{\partial u}{\partial x} \right]_{x=0}$$

Skin friction is calculated using Eq. (28), and an analytical formulation of non-dimensional friction drag is provided by

$$C_f = \frac{1}{\sqrt{B_1}} \frac{\tau^{\frac{\alpha}{2}}}{\Gamma(1 - \frac{\alpha}{2})} - \frac{B_2}{\sqrt{B_1}} \frac{\tau^{\frac{\alpha}{2}}}{\Gamma(1 + \frac{\alpha}{2})} + \frac{B_2}{B_1} \sqrt{\frac{pr}{A_{10}}} \frac{\tau^{\frac{\alpha}{2}}}{\Gamma(1 + \frac{\alpha}{2})}$$

where  $B = 1 + \frac{1}{\beta}, B_1 = BA_7, B_2 = -\frac{A_9A_{10}B_1Gr}{B_1 Pr - A_{10}}$  ... (33)

**Graphical results and observations**

The temperature, fluid flow derived for fractional (non-integer) order partial differential equations, and



flow characteristics involved in the problem are all graphically analyzed in this section. Analytical techniques, including the Laplace and Fourier sine transformations, are utilized to derive the flow model. The physical explanations for the time, thermal Grashof number, volume fraction, Prandtl number, thermal radiation parameter, and Casson parameter are explored. Because of the importance of shape effects, we assume that nanoparticles are hexahedron, blade, tetrahedron, lamina and cylinder. The impacts of different flow behaviours are analyzed by plotting the graphs in Figs. 2-17, which exemplify different effects on velocity field, energy, rate of heat transfer, and shear stress. Additionally, tables and bar graphs are used to analyze various aspects of fluid flow. To highlight the significance of fractional and classical models, this section also contains a visual comparison of the two types of solutions. In addition, a comprehensive table analysis is employed in order to investigate the Nusselt number as well as the friction drag.

### Effect of physical characteristics on the temperature field

The figures in this section are based on the temperature Eq. (10), its solution is shown in Eq. (22). The effect of the fractional variable on the thermal profile is depicted in Fig. 2. It has been witnessed that when the values of  $\alpha$  go higher, the thermal profile gets higher along with them. It is worth noting that increasing the order results in a large development of the memory effect included in the non-integer order, which has a special influence on the time values. We find that increasing the fractional order derivative causes a rise in time, which causes an increase in temperature depending on the kind of exact solution. Fig. 3 demonstrates the effect of time on the thermal profile. In the fractional scenario, the value of time progressively increases, which results in an increase in temperature. This implies that the Caputo derivative has less of an impact on the diffusion process as time approaches one. Fig. 4 illustrates the impact of the radiation parameter on the thermal field.

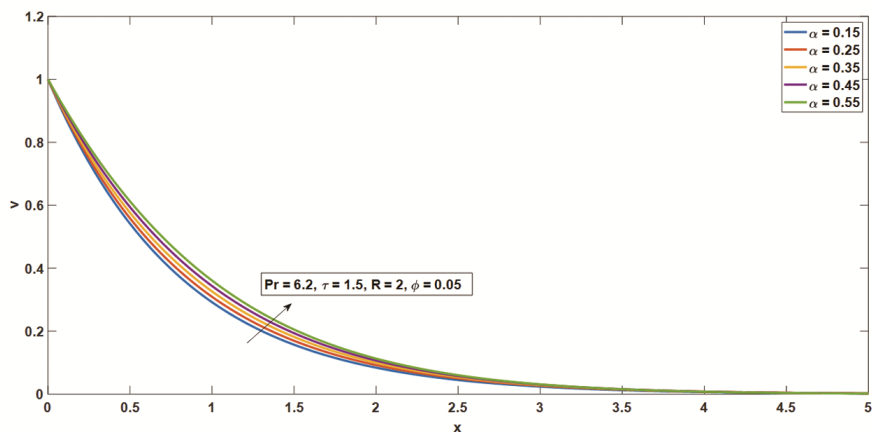


Fig. 2 — Temperature of the fluid for distinct  $\alpha$

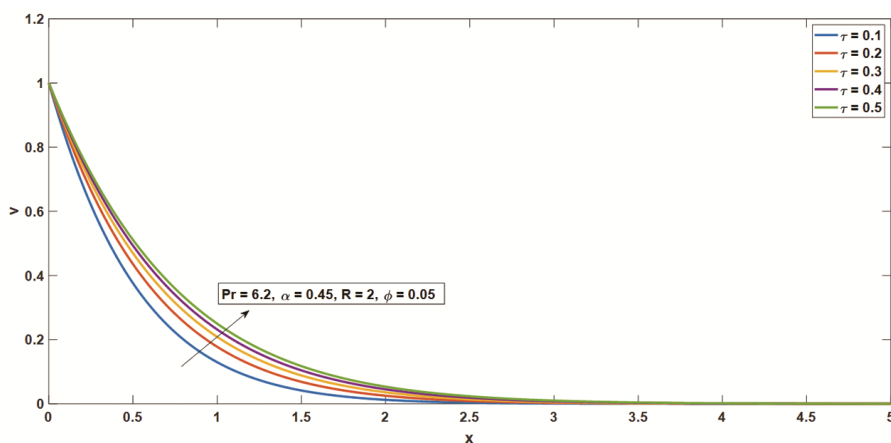


Fig. 3 — Temperature of the fluid for distinct  $\tau$

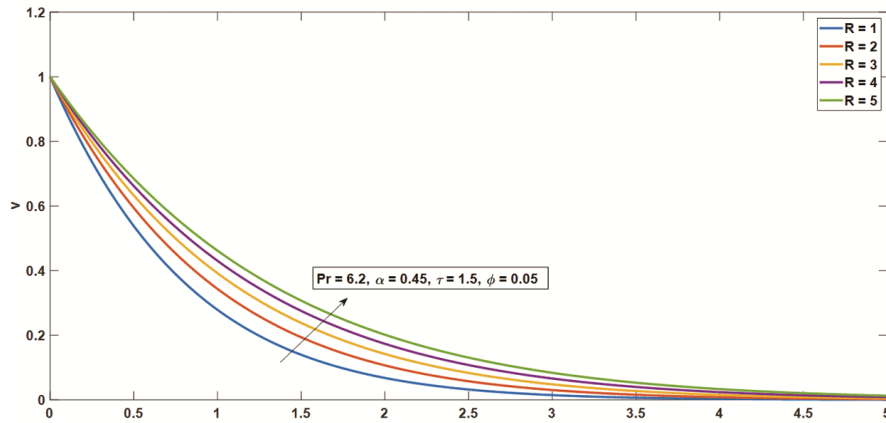
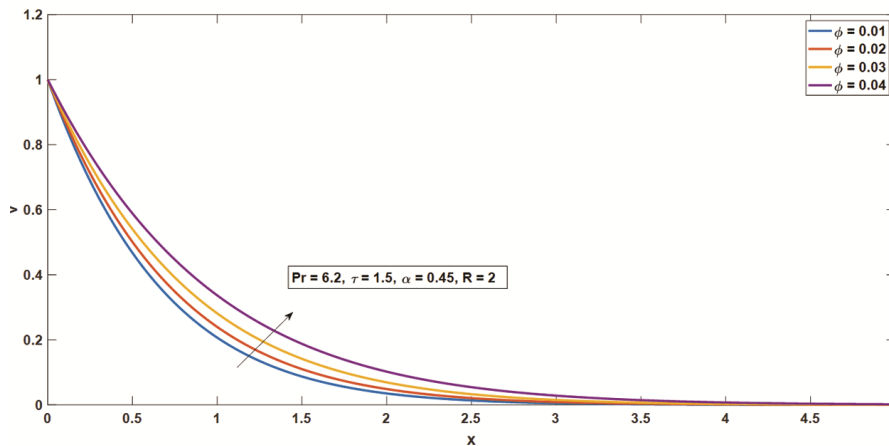


Fig. 4 — Temperature of the fluid for distinct R

Fig. 5 — Temperature of the fluid for distinct  $\phi$ 

Increasing R values results in an improvement to the thermal profile. This is because the coefficient of mean absorption decreases as R grows, and it is inversely proportional to R. Because radiative heat transmission is less effective than conductive heat transfer, the buoyant force is dropped. High R efficiently transfers more energy to working fluids, resulting in an increase in the thermal field. When R is increased, the fluid gets more heated. As a result, there is a substantial increase in heat transmission. The fluctuation in temperature distribution caused by variations in the aggregated volume fraction of nanoparticles is investigated using Fig. 5.

The temperature function graph begins to rise as the nanoparticle ( $Fe_3O_4$  and  $CuO$ ) net volume fraction increases from 1% to 4%, as shown in the figure. This result is mostly due to the substantial thermal properties of  $Fe_3O_4$  and  $CuO$  nanoparticles, which improve the rate of heat transfer of the base fluid. As a consequence of these thermal qualities

assisting the base fluid in gaining excess energy, the graph of temperature variation attains high levels. Fig. 6 represented the temperature distribution for different nanoparticle morphologies. The shape factor shown in Table 3 reveals that lamina-shaped nanoparticles have the greatest temperature field, followed by those with blade, cylinder, tetrahedron, and hexahedron geometries. It is important to keep in mind that viscosity reduces with increasing temperature. The viscosity of tetrahedrons, cylinders, and blades is obvious, leading to lower temperatures, but hexahedrons and laminas have the highest temperature owing to their minimal viscosity. The image also illustrates that the nanoparticle's hexahedron structure has a low viscosity. This is because of temperature dependent shear thinning.

#### Effect of physical characteristics on the flow field

The figures in this section are based on the temperature Eq. (9), whose solution is shown in Eq. (28). Different fractional order scenarios are used

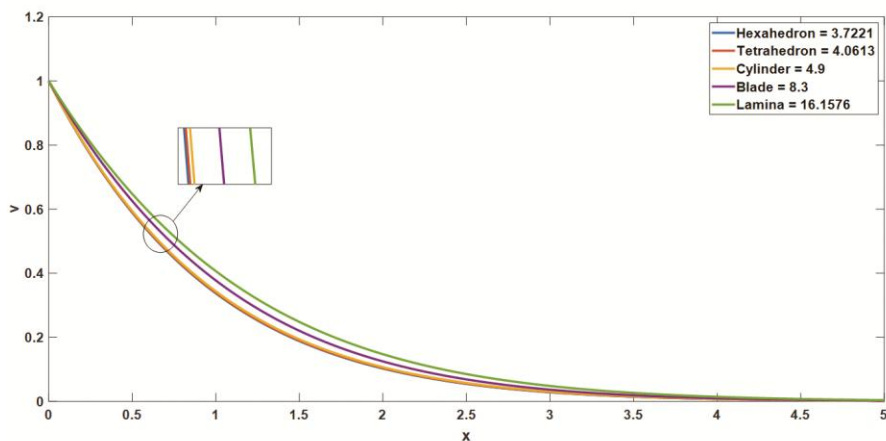


Fig. 6 — Temperature of the fluid for different shapes

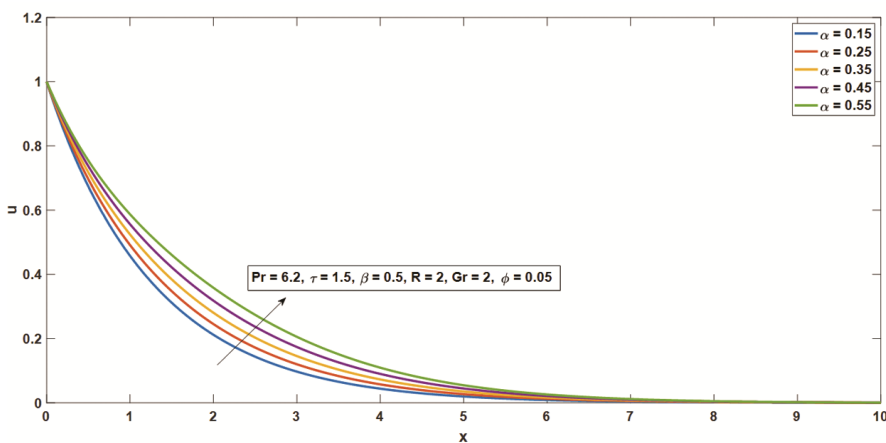


Fig. 7 — Curves of fluid flow for various  $\alpha$

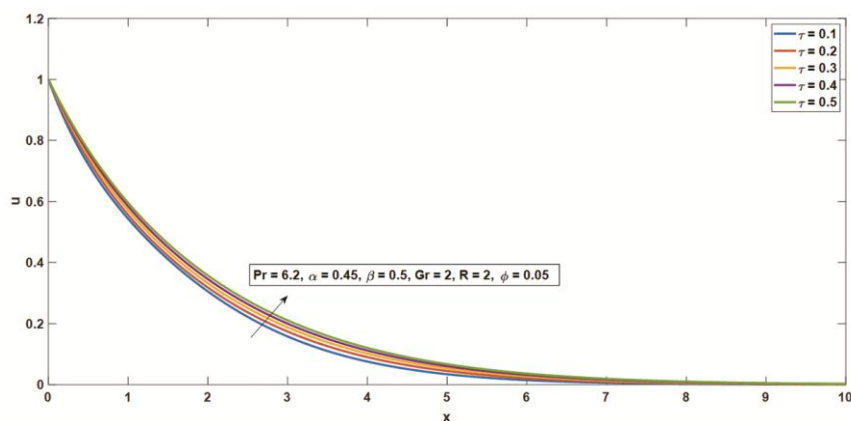


Fig. 8 — Curves of fluid flow for distinct  $\tau$

to show the dynamics of velocity for various flow conditions. In Fig. 7, we see the influence of fractional order as a function of time. When the order of the Caputo derivative rises, velocity falls. That is to say, as order  $\alpha$  increases, velocity decreases until it

reaches zero. The impact of time on the flow field is seen in Fig. 8, the velocity grows steadily as time progresses. When other variables are kept constant, Fig. 9 displays the effects of the Casson parameter. It demonstrates how fluid velocity tends to decrease as

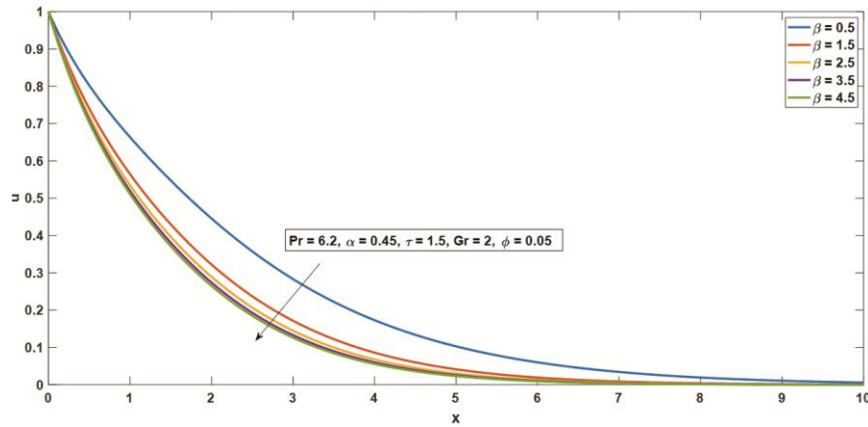


Fig. 9 — Curves of fluid flow for distinct  $\beta$

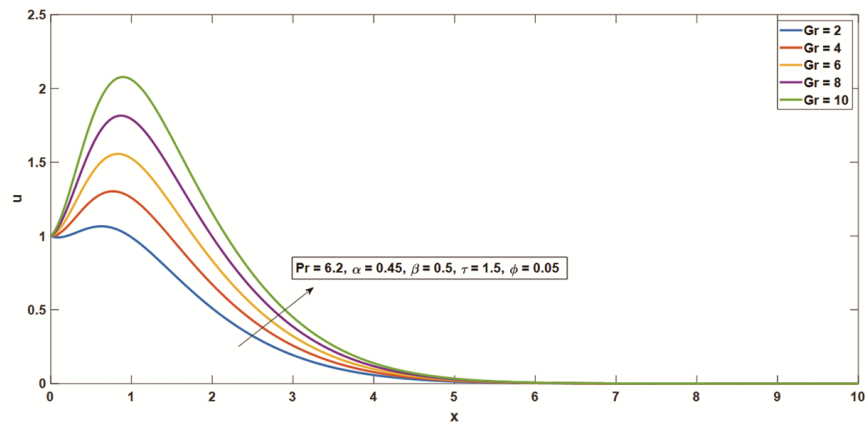


Fig. 10 — Curves of fluid flow for distinct Gr

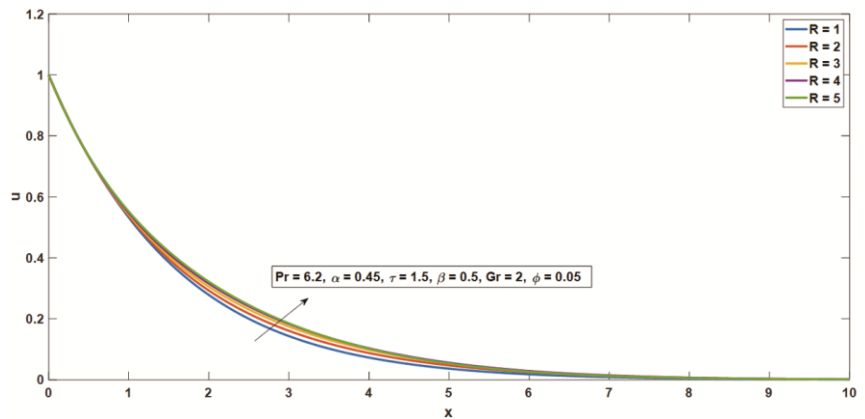
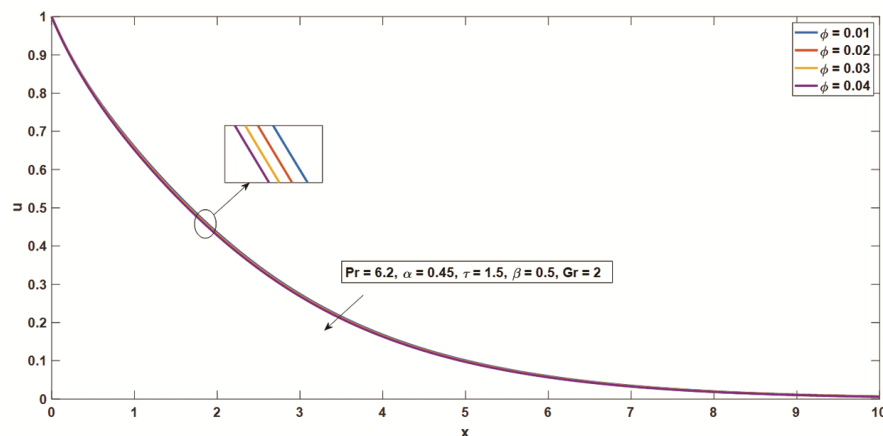
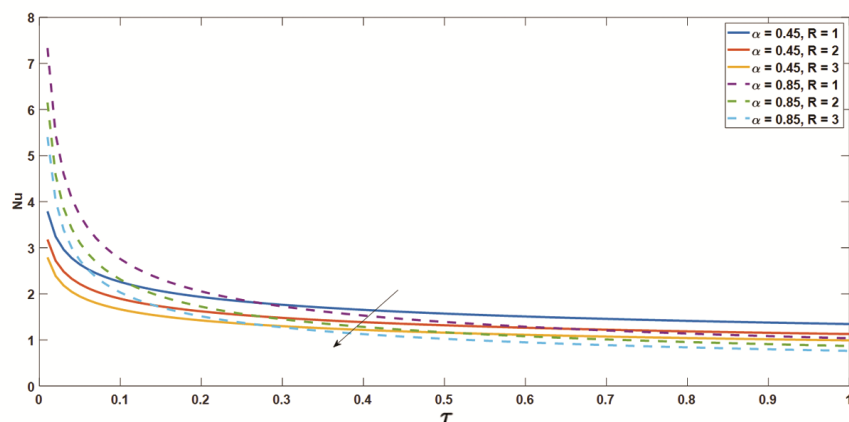


Fig. 11 — Curves of fluid flow for distinct R

Casson parameter values increase. This is due to the fact that a higher value of  $\beta$  will increase viscous forces while lowering thermal forces. As a result, the velocity of the fluid will obviously decrease.

Fig. 10 portrays the effect of Gr on the flow distribution. The hybrid nanofluid velocity increases as Gr increases. Because fluid motion is proportional

to the buoyancy force, the Grashof number is the ratio of the buoyancy force to the viscous force acting on the fluid. The thermal Grashof number controls the rate of heat transfer in problems involving convection. This trend can be physically justified by higher values of Gr increasing the buoyancy forces, resulting in increased hybrid nanofluid velocity. Fig. 11 exhibits

Fig. 12 — Curves of fluid flow for distinct  $\phi$ Fig. 13 — Nusselt number variations for  $\alpha$ 

the effect of the thermal radiation  $R$  on flow transport. It is shown that when the radiation parameter  $R$  rises, so does the velocity, signifying that the flow is accelerated. It conforms to the physical logic that, as  $R$  increases, the fluid has less radiation contact with the momentum boundary layer. It is observed in Fig. 12 that when the volume fraction of hybrid nanofluids rises, the velocity profile of the hybrid nanofluids slows down. The decrease in the velocity profile of the nanofluid may be explained physically by the fact that the viscosity of the fluid increases as the volume fraction of the hybrid nanoparticles rises.

Fig. 13 reveals the heat transmission coefficient in aspects of the Nusselt number for distinct values of the fractional and thermal radiation variables. It is noted that the heat transmission rate decreases with a rise in the fractional variable. Fig. 14 displays the Nusselt number as a function of time. We can see that the Nusselt number for water ( $Pr = 6.2$ ) and air ( $Pr = 0.71$ ) increases with increasing  $R$  in the figure. It is

also seen that the Nusselt number for water is larger than that of air. The cause for this is because smaller values of the Prandtl number are equal to greater thermal conductivities, which allow heat to disperse away from the plate quicker than larger  $Pr$  quantities, resulting in a slower heat transmission rate. Fig. 15 unveils the variation of friction drag against time. It is also noticed that when the volume fraction rises, so does the skin friction coefficient. Fig. 16 illustrates the effects of all flow variables on the rate of heat transfer. Heat transmission rate variations are greater in the case of volume fraction, followed by time, Prandtl number, and fractional parameter. In contrast, the variance in radiation parameters is minimal. In order to illustrate the comparisons between the fractional (non-integer) and ordinary derivative approach of hybrid nanofluids, Fig. 17 displayed 3D visualizations for the temperature field for different parameters. The graph demonstrates that the temperature of fractional hybrid nanofluids is faster

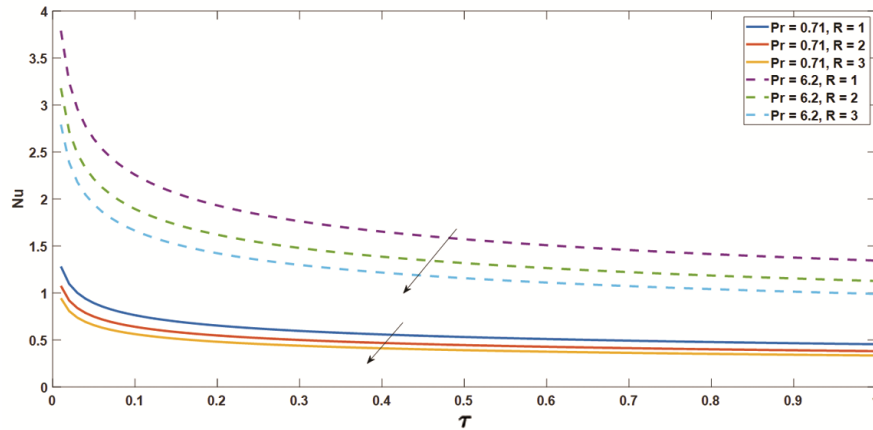


Fig. 14 — Nusselt number variation for Pr

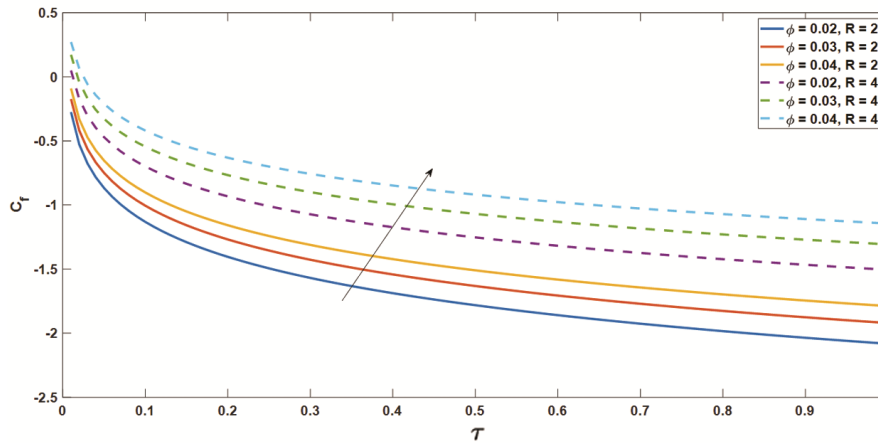


Fig. 15 — Skin friction variation for  $\phi$

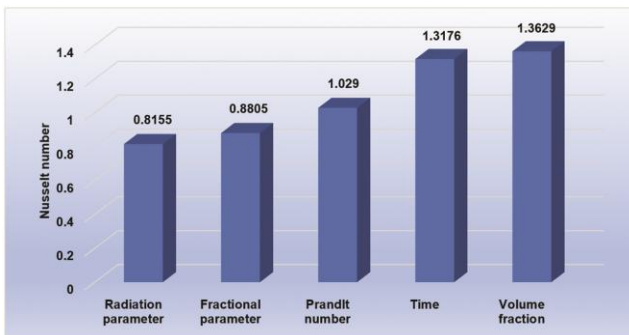


Fig. 16 — Nusselt number 3D graph with various parameters

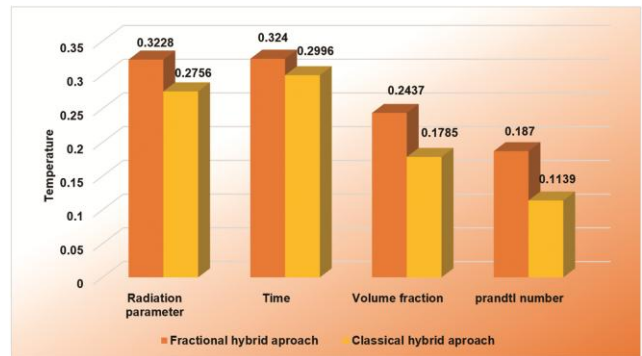


Fig. 17 — Comparison of fractional and classical hybrid nanofluid for temperature distribution

than that of ordinary hybrid nanofluids. It is shown that heat transmission is enhanced more by the fractional derivative model using hybrid nanofluids than by the conventional method.

Table 4 illustrates the influence of flow variables on the Nusselt number. Based on the table, increasing  $\phi_{Fe_3O_4}$ ,  $\phi_{CuO}$ , time  $\tau$ , radiation parameter R and

fractional parameter  $\alpha$  will cause a decrease in the rate of heat transfer, but an increase in Pr will result in an increase in the rate of heat transfer. The numbers in bold indicate that the Nusselt number in this row matches the parameter in this column. Table 5 displays the rate of heat transfer of various shapes of

Magnetite and Copper oxide nanoparticles. It is observed that hexahedron shaped nanoparticles show the highest heat transmission rate followed by tetrahedron, cylinder, lamina and blade shaped nanoparticles. The effects of different flow parameters on skin friction adjacent to a vertical plate are shown in Table 6. As shown here, rising  $\alpha$ ,  $\beta$ , Gr, R, Pr and  $\tau$  leads to decline of skin friction whereas increasing  $\phi_{Fe_3O_4}$  and  $\phi_{CuO}$  results in increment of skin friction.

### Validation of the results

By assuming the viscosity of Brinkman, the thermal conductivity of the Maxwell model, and using the numerical value of the thermophysical characteristics of nanomaterials from Table 1, the solutions obtained in temperature Eq. (22) can be reduced by setting ( $R = \phi = 0$ ) it to that of Ndolane Sene<sup>37</sup>. The solution presented in Eqs.(22),(28) from the present study and Eqs. (25), (28) from Ndolane

Table 4 — The Nusselt number's impact on the varies parameter

$\phi_{Fe_3O_4}$	$\phi_{CuO}$	Pr	$\alpha$	$\tau$	R	Nu
0.02	0.02	6.2	0.75	1.5	2	0.833630105239878
<b>0.03</b>	0.02	6.2	0.75	1.5	2	0.827574721379417
<b>0.04</b>	0.02	6.2	0.75	1.5	2	0.821550311495569
	<b>0.03</b>	6.2	0.75	1.5	2	0.826050005843931
	<b>0.04</b>	6.2	0.75	1.5	2	0.818514647819630
		<b>9</b>	0.75	1.5	2	1.004381720525542
		<b>12</b>	0.75	1.5	2	1.159760113429122
			<b>0.85</b>	1.5	2	0.756296600935403
			<b>0.95</b>	1.5	2	0.679458224293664
				<b>1.8</b>	2	0.778539089471265
				<b>1.9</b>	2	0.762912993982027
					<b>5</b>	0.597795600936625
					<b>6</b>	0.554579829249677

Table 5 — Nusselt number varies for various shape

$\phi_{Fe_3O_4}$	$\phi_{CuO}$	Hexahedron	Tetrahedron	Cylinder	Blade	Lamina
0.00	0.00	1.0995	1.0995	1.0995	1.0995	1.0995
0.01	0.01	1.0853	1.0844	1.0820	1.0734	1.0574
0.02	0.02	1.0711	1.0691	1.0644	1.0474	1.0162
0.03	0.03	1.0567	1.0538	1.0468	1.0214	0.9762
0.04	0.04	1.0423	1.0383	1.0290	0.9956	0.9377

Table 6 — The effect of the different variables on the skin friction

$\phi_{Fe_3O_4}$	$\phi_{CuO}$	Pr	$\alpha$	$\tau$	$\beta$	Gr	R	$C_f$
0.03	0.03	6.2	0.25	0.2	1.5	2	0.2	-1.521908677692061
<b>0.04</b>	0.03	6.2	0.25	0.2	1.5	2	0.2	-1.502805746900544
<b>0.05</b>	0.03	6.2	0.25	0.2	1.5	2	0.2	-1.487087469743950
-	<b>0.04</b>	6.2	0.25	0.2	1.5	2	0.2	-1.486004524819355
-	<b>0.05</b>	6.2	0.25	0.2	1.5	2	0.2	-1.454634621189193
-	-	<b>8</b>	0.25	0.2	1.5	2	0.2	-1.835238779035845
-	-	<b>9</b>	0.25	0.2	1.5	2	0.2	-1.995299088183070
-	-	-	<b>0.45</b>	0.2	1.5	2	0.2	-1.161809689236490
-	-	-	<b>0.75</b>	0.2	1.5	2	0.2	-0.688414952995501
-	-	-	-	<b>0.4</b>	1.5	2	0.2	-1.817916244082755
-	-	-	-	<b>0.6</b>	1.5	2	0.2	-1.997253351366399
-	-	-	-	-	<b>2.5</b>	2	0.2	-1.122462149719059
-	-	-	-	-	<b>4.5</b>	2	0.2	-0.802237584905219
-	-	-	-	-	-	<b>5</b>	0.2	-2.497632587906369
-	-	-	-	-	-	<b>7</b>	0.2	-2.822873891311139
-	-	-	-	-	-	-	<b>0.4</b>	-1.600426844808096
-	-	-	-	-	-	-	<b>0.6</b>	-1.665152078358084

Table 7 — Comparison result for temperature distribution when ( $R = \phi = 0$ )

Fractional parameter ( $\alpha$ )	Prandtl number ( $Pr$ )	Time ( $\tau$ )	Temperature for fractional case		Temperature for classical case ( $\alpha = 1$ )	
			Ndolane Sene <sup>37</sup>	Present result	Ndolane Sene <sup>37</sup>	Present result
0.85	6.2	0.5	0.0376	0.0415	-	-
<b>0.95</b>	6.2	0.5	0.0117	0.0287	-	-
	<b>9</b>	0.5	0.0193	0.0161	0.0027	0.0060
		<b>1.5</b>	0.1569	0.1800	0.1506	0.1877

Sene are computed and shown in Table 7. It is understood that the present results of the temperature field for fractional and classical cases exhibit good agreement in the study of Ndolane Sene. As a result, the author strongly recommends that the suggested mathematical model be used to examine the heat and fluid flow of the present situation.

**Conclusion**

Using the Caputo fractional derivatives, we develop a mathematical model for the free convective flow of a Casson fluid that includes nanoparticles of Magnetite and Copper oxide. Fourier sine and Laplace transforms are applied to provide precise outcomes. A few special solutions were found that are in line with the behavior of classical fluids and non-Newtonian fluids. The following inferences are drawn:

- The fractional results are transformed into classical solutions when  $\alpha = 1$ .
- Radiative heat flux is essential to the development of temperature and velocity fields.
- As a result of buoyancy force, the fluid flow rate tends to rise as the Grashof number increases.
- When the incremental volume fraction of  $Fe_3O_4$  and  $CuO$  nanomaterials is raised from 1 percent to 4 percent, the flow field graph decays; nevertheless, the behavior of the thermal profile is completely opposite.
- Because of the structure, material properties, and morphologies of the distributed nanomaterials, the resultant hybrid nanofluid is viscous in comparison to a typical fluid. Consequently, the boiling point of the hybrid nanofluid rises, resulting in increased thermal conductivity and heat transfer capability.
- The hybrid nanoparticles with lamina shapes are the most efficient in boosting the rate of heat transmission.

- When compared to classical models, the fractional model performs exceptionally well when it comes to explaining the memory effect.
- Compared to fluids with classic and fractional hybrid nanofluids, fractional hybrid nanofluids have the greatest heat transfer rate, while conventional fluid has the lowest. Thus, the fractional parameter enhances fluid flow.

**Nomenclature**

- $u$  Velocity (m/ s)
- $v$  Dimensionless temperature
- $U$  Fluid velocity
- $T$  Temperature ( $K$ )
- $Pr$  Prandtl number
- $Gr$  Grashof number
- $R$  Radiation parameter
- $t$  Time (sec)
- $k^*$  Coefficient of absorption
- $Fe_3O_4$  Magnetite nanoparticle
- $CuO$  Copper oxide nanoparticle
- $E_\alpha$  Mittag-Leffler function
- $x, y$  Cartesian coordinates
- $Nu$  Nusselt number
- $C_f$  Skin friction

**Greek symbols**

- $\rho_f$  Nanofluid density ( $kg\ m^{-3}$ )
- $(C_p)_f$  Nanofluid specific heat capacity ( $J\ kg\ K^{-1}$ )
- $(\gamma)_{nf}$  Nanofluid thermal expansion coefficient ( $K^{-1}$ )
- $\kappa_f$  Nanofluid thermal conductivity ( $W\ m^{-1}\ K^{-1}$ )
- $\mu_f$  Nanofluid dynamic viscosity ( $kg\ m^{-1}\ K^{-1}$ )
- $\rho_{hmf}$  Hybrid nanofluid density ( $kg\ m^{-3}$ )
- $(C_p)_{hmf}$  Hybrid nanofluid heat capacity ( $J\ kg\ K^{-1}$ )



- $(\gamma)_{hnf}$  Hybrid nanofluid thermal expansion coefficient  
( $K^{-1}$ )
- $\kappa_{hnf}$  Hybrid nanofluid thermal conductivity  
.....( $Wm^{-1}K^{-1}$ )
- $\mu_{hnf}$  Hybrid nanofluid dynamic viscosity ( $kg\ m^{-1}\ K^{-1}$ )
- $g$  Specific gravity ( $kg\ m^{-3}$ )
- $\alpha$  Fractional order parameter
- $\beta$  Casson fluid parameter
- $\Gamma$  Gamma Euler function
- $\sigma^*$  Stefan-Boltzmann constant
- $\tau$  Dimensionless time
- $\rho_f$  Density of the base fluid ( $kg\ m^{-3}$ )
- $\mu_f$  Viscosity of the base fluid ( $kg\ m^{-1}\ K^{-1}$ )
- $(C_p)_f$  Specific heat capacity of the base fluid  
( $J\ kg^{-1}\ K^{-1}$ )
- $\kappa_f$  Thermal conductivity of the base fluid  
( $W\ m^{-1}\ K^{-1}$ )
- $(\gamma)_f$  Thermal expansion coefficient of the base fluid  
( $K^{-1}$ )
- $\phi_1$  Volume concentration of  $Fe_3O_4$
- $\phi_2$  Volume concentration of  $CuO$

### Subscripts

- $F$  Base fluid
- $Nf$  Nanofluid
- $Hnf$  Hybrid nanofluid
- $Np$  Nanoparticle
- $W$  Wall
- $\infty$  Ambient condition

### References

- Choi S U S & Eastman J A, *Enhancing thermal conductivity of fluids with nanoparticles*(Technical report, Argonne National Lab, IL, United States), (1995).
- SPîslaru-Dănescu L, Morega A M, Telipan G, Morega M, Dumitru J B & Marinescu V, *IEEE Trans Magn*, 49 (2013) 5489.
- Bahiraei M & Hangi M, *Energy Conv Manag*, 76 (2013) 1125.
- Bash H T & Sivaraj R, *J Therm Eng*, 8 (2022) 38.
- Kumaran G, Sivaraj R, Subramanyam R A, Rushi K B & Ramachandra P V, *Europ Phys J Spec Top*, 228 (2019) 2647.
- Basha H T, Sivaraj R, Reddy A S, Chamkha A J & Tilioua M, *SN Appl Sci*, 2 (2020) 1.
- Yamada A, Sasabe H, Osada Y, Shiroda Y & Yamamoto I, *Concepts of Hybrid Materials, Hybrid Materials-Concept and Case Studies, ASM Int*, (1989).
- Shahzadi I & Nadeem S, *J Mol Liq*, 225 (2017) 365.
- Javadi H, Urchueguia J F, Mousavi A S S & Badenes B, *Energies*, 14 (2021) 2892.
- Ali R, Akgül A & Asjad M I, *Pramana J Phys*, 94 (2020) 131.
- Saqib M, Khan I & Shafie S, *Adv Differ Equ*, 52 (2019) 2019.
- Ul H S, Mahmood N, Jan S U, Khan I & Mohamed A, *Sci Rep*, 12 (2022) 19591.
- Khan M, Lone S A, Rasheed A & Alam M N, *Int Commun Heat Mass Transf*, 130 (2022) 105784.
- Kumar B & Srinivas S, *J Appl Comput Mech*, 6 (2020) 259.
- Jamil B, Anwar M S, Rasheed A & Irfan M, *Chinese J Phys*, 67 (2020) 512.
- Maiti S, Shaw S & Shit G C, *Phys A: Stat Mech Appl*, 540 (2020) 123149.
- Saeed S T, Khan I, Riaz M B & Husnine S M, *J Math*, 2020 (2020) 14.
- Reyaz R, Lim Y J, Mohamad A Q, Saqib M & Shafie S, *J Adv Res Fluid Mech*, 85 (2021) 145.
- Casson N, *Rheology Disperse Systems*, 10021830093 (1959) 84.
- Srinivas S, Kalyan K C, Badeti S & Reddy A S, 2022, October. MHD Flow of Casson Nanofluid Over An Inclined Porous Stretching Surface. In *Recent Advances in Applied Mathematics and Applications to the Dynamics of Fluid Flows: 5th International Conference on Applications of Fluid Dynamics (ICAFD)* (2020) 155. Singapore: Springer Nature Singapore.
- Arif M, Kumam P, Kumam W & Mostafa Z, *Case Stud Therm Eng*, 31 (2022) 101837.
- Wang F, Asjad M I, Zahid M, Iqbal A, Ahmad H & Alsulami M D, *J Mater Res Technol*, 14 (2021) 1292.
- Sarwar N, Asjad M I, Sitthiwiratham T, Patanarapeelert N & Muhammad T, *Symmetry*, 13 (2021) 2039.
- Krishna M V, Ahammad N A & Chamkha A J, *Case Stud Therm Eng*, 27 (2021) 101229.
- Kayalvizhi J, Vijaya K A G, Öztöp H F, Sene N & Abu-Hamdeh N H, *Energies*, 15 (2022) 6082.
- Jumarie G, *Comput Math Appl*, 51 (2006) 1367.
- Caputo M, *Geophys J Int*, 13 (1967) 529.
- Caputo M & Fabrizio M, *Prog Fract Differ Appl*, 1 (2015) 73.
- Atangana A & Goufo E D, *J Nonlinear Sci Appl*, 8 (2015) 763.
- Anwar T, Kumam P & Thounthong P, *IEEE Access*, 9 (2021) 12389.
- Raza A, Khan I, Farid S, My C A, Khan A & Alotaibi H, *Case Stud Therm Eng*, 28 (2021) 101373.
- Ahmad J, Ali F, Murtaza S & Khan I, *Math Probl Eng*, 2021 (2021) 12.
- Khan D, Kumam P, Khan I, Khan A, Watthayu W & Arif M, *Sci Rep*, 12 (2022) 6524.
- Saqib M, Mohd K A R, Mohammad N F, Chuan C D L & Shafie S, *Symmetry*, 12 (2020) 768.
- Ikram M D, Asjad M I, Akgül A & Baleanu D, *Alex Eng J*, 60 (2021) 3593.
- Lisha N M & Vijayakumar A G, *Symmetry*, 15 (2023) 399.
- Sene N, *Fractal Fract*, 6 (2022) 35.
- Shehzad S A, Hayat T, Qasim M & Asghar S, *Braz J Chem Eng*, 30 (2021) 187.

- 39 Nandkeolyar R, Seth G S, Makinde O D, Sibanda P & Ansari M S, *J Appl Mech*, 80 (2013) 061003.
- 40 Ali F, Khan I & Shafies S, *PLoS One*, 9 (2014) e85099.
- 41 Anwar T & Kumam P, *Case Stud Therm Eng*, 31 (2022) 101828.
- 42 Ali M E & Sandeep N, *Results Phys*, 7 (2017) 21.
- 43 Kumaresan E, Kumar A V & Kumar B R, Chemically reacting on MHD boundary layer flow of CuO-water and MgO-water nanofluids past a stretching sheet in porous media with radiation absorption and heat generation/absorption, *IOP Conference Series: Mater Sci Eng*, (2017).
- 44 Farooq U, Tahir M, Waqas H, Muhammad T, Alshehri A & Imran M, *Sci Rep*, 12 (2022) 12254.
- 45 Curtis W D, Logan J D & Parker W A, *Linear Algebra Appl*, 47 (1982) 117.
- 46 Sene N, *Chaos Solitons Fractals*, 117 (2018) 68.
- 47 Abro K A, Khan I & Gómez-Aguilar J F, *J Braz Soc Mech Sci Eng*, 41 (2019) 1.
- 48 Podlubny I, *Math Sci Eng*, 198 (1999) 41.